

Transient evolution of shear-banding wormlike micellar solutions

Erik Miller, Jonathan P. Rothstein*

Department of Mechanical Engineering, University of Massachusetts, Amherst, MA 01003-2210, USA

Received 1 August 2006; received in revised form 10 November 2006; accepted 23 December 2006

Abstract

A series of experiments were performed to further investigate the phenomenon of shear-banding in surfactant solutions. Many surfactant solutions, through their unique amphiphilic chemistry, form long wormlike micelle structures which behave like living polymers. These wormlike micelles have interesting viscoelastic properties and have been the subject of a number of recent studies. These water-based surfactant systems are widely used in many commercial and industrial applications; however, many aspects of their complex flow behavior are still not fully understood. In this study, a Couette cell was designed to allow for high-resolution optical access in a simple shear flow of a surfactant system comprised of cetylpyridinium chloride and sodium salicylate in aqueous sodium chloride. Beyond a critical stress, this system is found to enter a non-linear regime in which there is a plateau in the shear stress with increasing shear rate. Within this plateau, the fluid forms distinct bands of varying shear rate. The goal of this study was to obtain high spatial and temporal resolution particle-image velocimetry and flow-induced birefringence results in both steady and transient-startup flows. As a consequence of the high resolution, steady PIV results suggest the existence of multiple-shear bands. In the transient PIV experiments, we observe a propagating damped elastic wave, as well as fluctuations in the shear-band evolution on timescales of less than one relaxation time. Pointwise FIB gap profiles show a diffuse birefringent region prior to the onset of shear-banding in the velocity profiles. These results provide insight on the flow behavior, as well as a full set of experimental data which will drive development of constitutive models capable of predicting shear-banding.

© 2007 Elsevier B.V. All rights reserved.

Keywords: Flow-induced birefringence; Particle-image velocimetry; Shear-banding; Surfactant solutions; Wormlike micelles

1. Introduction

1.1. Wormlike micelle solutions

Surfactants are used in a variety of applications that benefit from their unique viscoelastic properties, including many household and cosmetic products, industrial viscosity modifiers, emulsifiers, encapsulants, and lubricants. In addition to these more common and recognizable products, scientists have been researching the use of viscoelastic surfactant technology for use as polymer-free aqueous fracturing fluids in oilfield applications including drilling and reservoir stimulation [1]. Surfactants have many interesting properties as a result of their unique chemical structure. The basic surfactant molecule is amphiphilic, whereby it possesses both hydrophilic (water-loving) and hydrophobic or lyophilic (water-fearing or oil-loving) groups that are chemi-

cally bonded together. Typical lyophilic groups are slender but relatively short hydrocarbon chains with a length of 8–20 carbon atoms and are often referred to as the surfactant ‘tail’. The hydrophilic group, in contrast, is short and bulky and therefore referred to as the ‘head’ [2]. Depending on the exact chemical makeup of the molecule, surfactants can also have a positive, negative, or neutral charge; cationic, anionic, and nonionic, respectively. When placed in water at a high enough concentration known as the critical micellar concentration (CMC), surfactant molecules will self-assemble into large aggregates known as micelles in such a way that the tails become closely packed together in order to minimize their exposure to water. Based on several factors including the type of solvent, surfactant concentration, and ionic strength, micelles can take the form of spheres, cylinders or even more complex and highly ordered aggregates such as vesicles and bilayers. A schematic diagram of typical surfactant micelle morphologies is included in Fig. 1.

Cylindrical micelles can grow into very long wormlike micelles with increasing surfactant concentration. Because of their long flexible structure, these worms can tangle around each other and form a complex network, much like polymer chains.

* Corresponding author.

E-mail addresses: ermiller@ecs.umass.edu (E. Miller), rothstein@ecs.umass.edu (J.P. Rothstein).

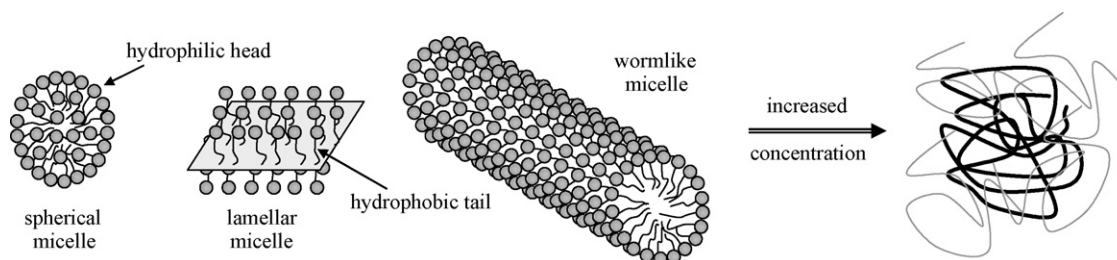


Fig. 1. Schematic diagram of self-assembled surfactant micelle morphologies.

However, unlike polymers that have covalently bonded hydrocarbon backbones, a wormlike micelle is only held together by relatively weak physical attractions/repulsions which break and reform with time. The dynamics of this ongoing and reversible breakup and reformation process is a strong function of surfactant and salt concentration, salinity, temperature, and flow. For this reason, wormlike micelles are commonly referred to as living or equilibrium polymers [3]. This continuous breaking and reforming gives networks of wormlike micelles an additional mechanism for relaxing from a stressed state back to a random walk equilibrium conformation. In an entangled network, both individual polymer chains and wormlike micelles can move past each other through reptation driven by Brownian motion. In addition to reptation, and unlike polymer chains, wormlike micelles can move past confinement points by breaking [4]. The reptation and breakup relaxation mechanisms have characteristic time scales of λ_{rep} and λ_{br} , respectively. Entangled wormlike micelle solutions display an additional interesting property in the fast-breaking limit where the breakup time is much shorter than the reptation time, $\lambda_{\text{br}} \ll \lambda_{\text{rep}}$ [5]. In this regime, typical of small amplitude oscillatory shear flows, where deformation is linear and the scission of micelles is reversible, wormlike micelles are nearly ideal Maxwell fluids with a single relaxation time, λ_M . Cates showed this single relaxation time is the geometric mean of the reptation and breakup times, $\lambda_M = (\lambda_{\text{rep}}\lambda_{\text{br}})^{1/2}$ [6].

The rheological behavior of wormlike micellar solutions is very similar to that of viscoelastic polymer solutions [4]. However, the ability of these micelle solutions to break, reform, and modify their morphology in response to a flow can lead to some very interesting phenomena when they are placed in various non-linear flow conditions. In some viscometric flows, shear-thickening behavior followed by the onset of a flow instability has been observed [7]. New and different flow instabilities have also been observed in the strong extensional flow following the wake of a falling sphere [8]. In transient uniaxial extension using a filament stretching rheometer, wormlike micelle solutions exhibit significant strain-hardening similar to many polymer solutions. Unlike polymers, however, which undergo eventual failure via elastocapillary thinning, the wormlike micelle solutions fail through a dramatic rupture attributed to the scission of micelles that is found to be independent of extension rate [9]. In other shear flows, wormlike micelle solutions form banded structures of differing surfactant morphologies having vastly different rheological properties [2,10]. This class of behavior has been attributed to shear-induced structure formation, shear-induced phase change from isotropic to nematic phase, as

well as shear-induced gelation and mixing. This shear-banding behavior will be discussed in detail in the following section.

1.2. Shear-banding in wormlike micelle solutions

The unusual dynamics of surfactant wormlike micelles have been studied in shear flows of varying geometry for many years. In a steady shear flow at low shear rates, wormlike micelles behave like a Newtonian fluid with a constant viscosity independent of shear rate. As the shear rate is increased, the viscosity begins to shear thin. Above a characteristic shear rate, the shear stress becomes nearly constant and independent of the imposed bulk shear rate [11]. This plateau in shear stress can extend over multiple decades in shear rate before hitting a high shear rate branch and once again increasing monotonically with shear rate. Within this stress plateau, and given proper flow conditions, distinct bands of fluid at different local shear rates can develop. The relative proportions of these physical bands are the subject of much recent research. Fundamentally, it is clear that the high and low shear-rate bands at a constant stress form in response to the need to preserve an average rate of strain across the flow profile [10]. Shear-bands have been observed using several predominantly optical methods including flow-induced birefringence (FIB) [12–14], particle-image velocimetry (PIV) [15–17], light and small-angle neutron scattering (SANS) [7,18,19], and nuclear magnetic resonance (NMR) imaging [10,20].

In a given flow, as the shear rate increases to some maximum or critical level, $\dot{\gamma}_{\text{crit}}$, the fluid may relax down to and maintain the shear stress plateau by forming bands which can coexist at different shear rates. In this manner, the majority of the shear rate can be taken up by a smaller fraction of the fluid. The average of the local shear rates in the bands must be that of the applied bulk shear rate, where the proportions are described by a simple lever rule [10,20]:

$$\dot{\gamma} = \alpha_1 \dot{\gamma}_1 + \alpha_2 \dot{\gamma}_2, \quad \text{where } \alpha_1 + \alpha_2 = 1. \quad (1)$$

A mechanical rheometer can only measure stress and the average shear rate across the entire sample. For this reason, rheometry results are observed as the plateau seen in Fig. 2, followed by a transition to the upper shear branch once the shear rate in the sample is high enough [20].

There is a great deal of research aimed at elucidating the size distribution and nature of the shear-bands which are formed in flows of wormlike micelles. Eq. (1) does not give any insight about the size of the bands or even how many bands may

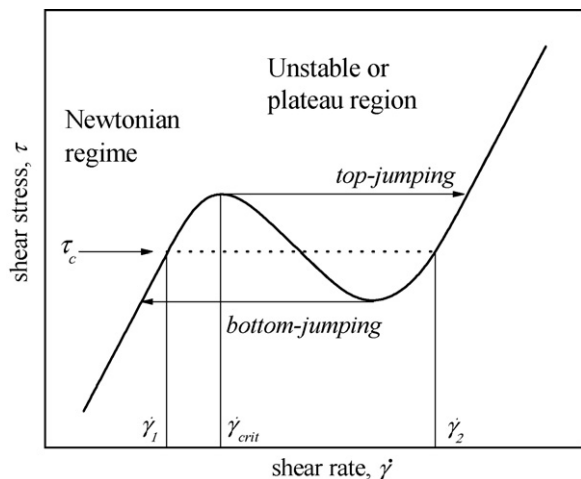


Fig. 2. Schematic representation of a flow curve exhibiting plateau behavior indicative of shear-banding.

exist within the plateau region, it simply constrains the volume fraction in each band. Some numerical calculations seem to suggest two or even three bands can exist, but the size and precise location of these bands is still undetermined [20]. The early theory of Doi and Edwards [21] predicts nonmonotonic behavior in polymers that become aligned along the flow direction at high shear rates and can no longer generate a shear stress. Cates [3] later extended their work to wormlike micelles by incorporating breakup dynamics and a time-evolving spectrum of micelle lengths. The Cates constitutive model results in a good prediction of the observed shear stress in cetylpyridinium chloride/sodium salicylate (CPyCl/NaSal) systems [22] and produces a nonmonotonic flow curve, shown in Fig. 2 as a solid line. While the Cates model furthers our physical understanding of what is seen in mechanical rheometers, because it is an integral model, it is only tractable in simple flow calculations. Thus, there is a direct need for a differential constitutive model that can not only predict the bulk mechanical measurements, but also identify the number, position and strength of the resulting shear-bands.

While the plateau (dashed line in Fig. 2) is most common, some experiments show a hysteretic behavior in controlled stress situations. Top-jumping occurs when the flow curve jumps to the high shear branch directly from $\dot{\gamma}_{crit}$ in an increasing stress experiment, and bottom-jumping when the same flow curve is followed down below the plateau, then jumps to the low shear rate branch. Extended from the Cates model, theoretical work with a nonmonotonic constitutive relation confirms the existence of banded flow, but with indefinitely narrow width [23]. This is an unphysical result; however, it can be avoided by adding terms to account for inhomogeneous states within the flow. This result gives a high and low shear-band state and suggests that the banded flow is a partial result of different phases or morphologies within the fluid [23]. More recent numerical work has been performed using the framework of the two-fluid model [24–26]. This approach eliminates the need for adding terms in an *ad hoc* manner to the Cates model and provides a direct coupling between stress and composition [12]. Full 2D and 3D

simulation results have been reported in this collected body of work and have provided a framework for the existence of the shear-banding instability in wormlike micellar solutions. The results also suggest that the constitutive instability is coupled with a phase transition [12]. However, there exist relatively few experimental studies which can provide data to validate these results.

The nonmonotonic shear-banding behavior has been attributed to the formation of different phases in the fluid by many researchers. Cappelaere et al. [27] used both shear- and stress-controlled rheology, along with flow birefringence and SANS to show that a concentrated wormlike system of cetyltrimethylammonium bromide (CTAB) undergoes a first-order isotropic to nematic phase transition induced by shear. In their study, the rheology confirms the stress plateau, flow birefringence allows visualization of the distinct high and low shear-bands, and SANS can provide information about the phase. The work of Berret et al. [18,28,29], using highly concentrated solutions of CPyCl/NaSal in an aqueous sodium chloride (NaCl) solution, provides a great deal of evidence on a phase transition in the wormlike system. The first-order isotropic to nematic transition is accounted for by a simple nucleation and one-dimensional growth model. Physically, this mechanism proposes that different phases of micelles are present within the high and low shear-bands. In steady experiments, the CPyCl/NaSal solutions of Berret et al. in fact show two phases which are stable, but have differing viscosity, orientation, and order parameters [28]. Transient rheology has further shown that the flow mechanisms for shear-banding are very complex [14]. Observations have shown that there is a first mechanism that occurs on the scale of a single relaxation time, λ_M , where the micelles behave like a conventional elastic polymer, with a stress overshoot and damped oscillations at higher strain rates. A second mechanism occurs over much longer time scales and manifests itself as a longtime sigmoidal relaxation with a transition from homogeneous to inhomogeneous flow; a phase transition from isotropic to nematic [11].

In more dilute solutions of wormlike micelles, the isotropic and nematic phase transitions are very distant on the phase diagram, and a shear-induced phase transition is unlikely [19]. However, results using a two-fluid model show that flow-induced phase separation can, in fact, occur in semi-dilute micellar solutions that are far from the phase transition [12]. The two phases of fluid can have vastly different properties, including moduli and relaxation times, which play an important role in dynamical phase behavior. A large dynamic contrast between the two phases can account for a large shift in the equilibrium phase boundary [12]. Essentially, there exists a different phase diagram for a dynamic flow scenario than that for the system at rest.

The stress plateau and shear-band are indicative of behavior seen in less concentrated CPyCl/NaSal systems, primarily the Rehage and Hoffman model 100 mM/60 mM system in water [4,10,15,30–33]. It is therefore less clear whether flow-induced phase separation is in fact the driving force for shear-banding [12], or simply another feature. Some evidence of longer timescale effects has been seen in these less dilute systems as

well. Long-time transient rheology shows that in terms of shear stress, the relaxation of a metastable state to a true steady state occurs on a scale much longer than a single Maxwell relaxation time for the fluid. While this behavior is similar to what was reported previously [29], where the results are attributed to nucleation and growth of a shear-induced nematic phase, it is unlikely that the same is true for solutions at lower weight fractions. Still, regardless of whether the high shear-band has nematic order, which it most likely does, the issue remains whether the banding instability is caused by a flow-induced perturbation to the phase transition, or is a purely mechanical flow instability [34]. We concede that the distinction between these viewpoints is not altogether concrete.

Another viewpoint from recent studies suggests that the CPyCl/NaSal systems do not truly exhibit the phenomenon known as shear-induced phase separation (SIPS) [19]. It has been shown with some certainty that this particular class of wormlike micellar systems experience shear-banding with a highly aligned nematic-like state in the high shear-band [14,16]. In contrast, however, SANS measurements of other micellar systems have proposed a more accurate SIPS in which a striated system of micron-sized bands of highly branched and concentrated micelles coexist with a nearly isotropic brine phase [19].

As part of a collaboration to explore new constitutive models that will accurately predict and model shear-banding in wormlike micellar systems [35,36], the goal of our research is to build on the work of the aforementioned scientists by collecting high resolution temporal and spatial data of shear-band development. Our experiments focus on providing data to fit and match with new theory. This manuscript will detail the efforts in visualizing the shear-bands through velocity profile and flow-induced birefringence measurements having dramatically improved spatial and temporal resolution from the studies currently in the literature. With respect to the previous work, shear-bands are often small and several methods such as NMR do not have the spatial resolution to capture dynamics in developing bands; in some cases it is rare to capture more than one data point in a high shear-band. Furthermore, with characteristic time scales on the order of 1 s or less, increased temporal resolution may also elucidate the subtleties of how the shear-bands develop, grow, and behave over time in various flow conditions. Both steady and transient flow experiments are used to explore the shear-banding behavior.

The outline of this paper is as follows. In Section 2 we will describe our Couette shear cell and implementation of particle-image velocimetry and modulated flow birefringence, as well as provide details on the test fluid system. In the results section, we will discuss our collective results, including velocity profiles and birefringence, both steady and transient. Finally, we conclude with some remarks on the shear-banding mechanism.

2. Experimental

2.1. Working material

The material chosen for this study is the system made up of the cationic surfactant cetylpyridinium chloride (CPyCl), where

the surfactant ion is cetylpyridinium (CPy⁺), and the strongly binding salicylate counterion (Sal[−]) from sodium salicylate (NaSal). This system is well studied and known to form elongated wormlike micelles. The classic system of CPyCl/NaSal at a concentration ratio of [100 mM/60 mM] was found to be optimal through a series of experiments varying the counterion concentration [4]. In the interest of varying the surfactant concentration to observe various effects, the ratio $R = [\text{CPy}]/[\text{Sal}]$ was chosen and kept constant at $R=2$, based on a similar approach in a viscoelastic study of another common surfactant [37]. The decision to use less NaSal is based on the structure which is formed. Sal[−] is a large ion and positions itself between CPy⁺ surfactant ions in the micellar structure. Optimal spacing and long slender wormlike structure is achieved in this specific case for $R > 1$. This ratio, however, creates an electrostatic imbalance so the system is dissolved in a somewhat concentrated salt solution (aqueous NaCl, 100 mM). The dissociated salt provides constant electrostatic screening for the non-equimolar CPy/Sal system while surfactant concentration is varied and thereby enhances the entanglements and viscoelasticity. This electrostatic screening effect is further supported by the observation that the CMC for CPyCl in aqueous NaCl, $\text{CMC}_{\text{CPy,NaCl}} = 0.12 \text{ mM}$, is almost a full order of magnitude lower than that of water, $\text{CMC}_{\text{CPy,H}_2\text{O}} = 0.90 \text{ mM}$ [12]. Furthermore, the linear and monotonic viscosity behavior of CPyCl/NaSal in the semi-dilute regime has also been well characterized with a transition from dilute to semi-dilute at $[\text{CPy}] = 18 \text{ mM}$ [38].

CPyCl and NaSal were obtained in dry form from Fisher Scientific and solutions were mixed by molarity. Measured amounts were dissolved in the aqueous NaCl solution, on a hot plate with a magnetic stirring bar. During mixing, a moderately elevated temperature of 40–50 °C was applied to reduce viscosity and aid in uniform mixing. After the solutions were fully dissolved, approximately 20–30 min, they were allowed to stand at room temperature for at least 24 h before any experiments were performed to allow air bubbles introduced during mixing to rise out. Dynamic small-amplitude oscillatory shear (SAOS) and controlled ramps of both steady shear-rate and shear-stress were performed for a wide range of surfactant concentrations at a constant molar ratio of $R=2$ to confirm that the linear viscoelasticity of our samples were inline with previous studies. Additionally, the concentration of salt (NaCl) was varied to confirm the appropriate degree of electrostatic screening. It was determined that 100 mM NaCl was sufficient, as there was no detectable difference in the rheology with higher concentration NaCl for the more concentrated surfactants used in this study. It should be noted that too much excess salt can affect the rheological behavior by inducing crosslinking of the wormlike micelles [39]. Based on historical results as well as a practical compromise between viscoelastic behavior and practical/usable viscosity (this relates to the loading of the test cell and will be discussed more in the following section) the model system was identified as 100 mM/50 mM CPyCl/NaSal dissolved in an aqueous solution of 100 mM NaCl. Additionally, 50 and 200 mM CPyCl with the same molar ratio of $R = 2$ and in the same aqueous salt were selected to probe above and below the model 100 mM system.

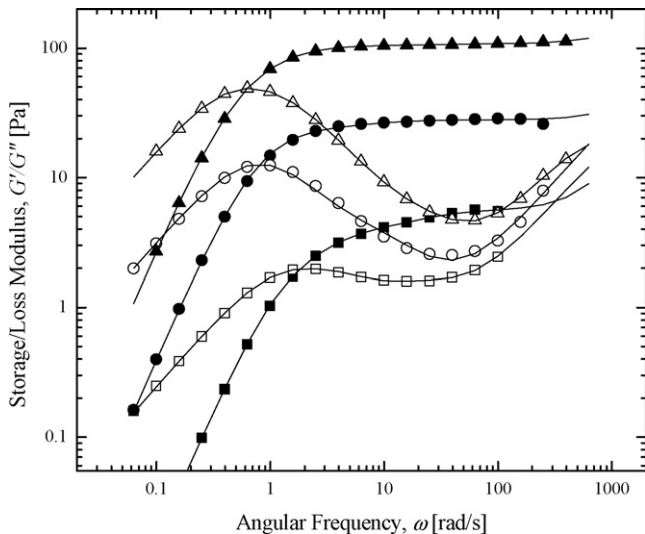


Fig. 3. Dynamic SAOS rheology of CPyCl/NaSal [$R=2$] solutions in 0.1 M NaCl at $T=20\text{ }^{\circ}\text{C}$. The data include: storage modulus, G' (filled symbols), and loss modulus, G'' (open symbols), for 50/25 mM (■), 100/50 mM (●), and 200/100 mM (▲), with lines representing multi-mode Maxwell fits to the data.

Rheology experiments were performed using a stress-controlled rheometer (TA instruments, AR2000) with a $6\text{ cm}/2^{\circ}$ cone-and-plate geometry at $20\text{ }^{\circ}\text{C}$. The results of the dynamic and steady rheology are shown in Figs. 3 and 4, respectively. The linear viscoelasticity data in Fig. 3 were fit using a discrete multi-mode Maxwell spectrum. While many wormlike systems can be modeled with a simple one-mode Maxwell model, a satisfactory fit to the dynamics in this case was obtained using two modes. The primary mode corresponds to the crossover in G' and G'' and is the reported Maxwell relaxation time, λ_M , for this system. The much higher frequency mode describes the upturn in G'' resulting from Rouse-like high frequency breathing modes of the chain within its tube of confinements. The two modes correspond loosely to the dual nature of stress relaxation in wormlike

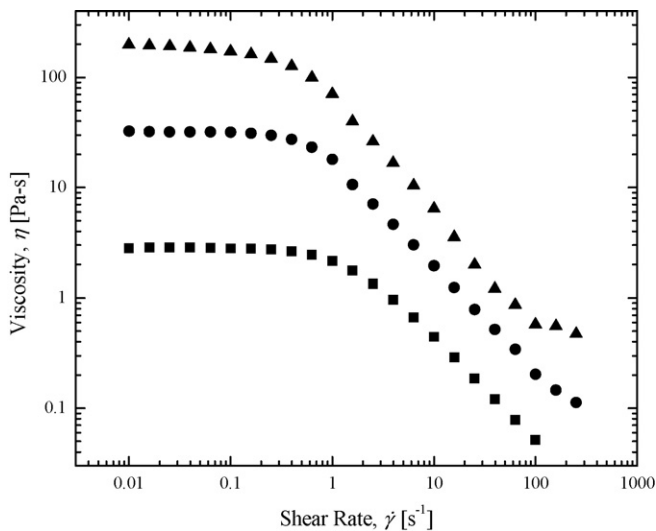


Fig. 4. Steady-shear rheology of CPyCl/NaSal [$R=2$] solutions in 0.1 M NaCl at $T=20\text{ }^{\circ}\text{C}$. The data include viscosity for various concentrations: 50/25 mM (■), 100/50 mM (●), and 200/100 mM (▲).

Table 1
Properties of CPyCl/NaSal solutions at $T=20\text{ }^{\circ}\text{C}$

	CPyCl/NaSal (mM)		
	50/25	100/50	200/100
Zero-shear viscosity, η_0 (Pa s)	2.84	31.5	196
Plateau modulus, G_0 (Pa)	4.2	27	104
Maxwell relaxation time, λ_M (s)	0.77	1.44	1.69
Micelle breakup time, λ_{br} (s)	0.05	0.04	0.01
Density, ρ (kg/m^3)	1030	1045	1090
Mesh size, $\xi_m = (kT/G_0)^{1/3}$ (nm)	42.3	22.7	14.5
Elastic wave speed, $C = (G_0/\rho)^{1/2}$ (m/s)	0.064	0.161	0.309
Critical Weissenberg#, $Wi_{crit} = \dot{\gamma}_{crit}\lambda_M$	3.4	2.0	1.6

micelles. The crossover frequency of the slower mode is the reciprocal of what is often reported as the single-mode Maxwell relaxation time. The higher frequency mode from this fit corresponds to a much smaller timescale and is also in good agreement with the breakup time of the wormlike micelles, λ_{br} , as estimated by using the observed deviation from Maxwellian behavior on a Cole-Cole plot [40] and reported in Table 1.

Steady-shear rheology was performed in a controlled shear rate experiment. In Fig. 4, constant-viscosity Newtonian behavior is seen at low shear rates, followed by a shear thinning regime with a slope of approximately $\eta \propto \dot{\gamma}^{-1}$. This corresponds with a plateau in the shear stress, and will be discussed in a following section. Additional parameters that are extracted from the rheology are listed in Table 1. They include the plateau modulus, G_0 , and the zero-shear rate viscosity, η_0 . Density was measured for all three fluids, and is slightly higher than that of water, as expected. Using these parameters, the theoretical mesh size or the correlation length of the entangled network, $\xi_m = (kT/G_0)^{1/3}$ [21,41], can be calculated and gives an estimate for the proximity of entanglements and density of the mesh. The elastic wave speed, $C = (G_0/\rho)^{1/2}$, is also calculated based on the system's density and elastic plateau modulus. The significance of the elastic wave speed will be discussed in a later section as it pertains to the velocity profile development.

2.2. Test apparatus: design and construction

It was necessary to design a flow cell with clear optical access for the velocity profile and flow-induced birefringence measurements. In order to achieve high spatial resolution, a physically large device was used to maximize the number of measurements that could be taken within the flow. A Couette flow cell with a rotating inner cylinder was selected for its ability to produce a simple shear flow continuously for a fixed volume of fluid, relative ease of construction, and ability to allow for visualization through the gap between the two cylinders. Similar devices have been used in previous studies [12,42]. A schematic of our specifically designed Couette cell is shown in Fig. 5.

Both cylinders were fabricated from acrylic, with the bob having a radius of $R_{inner} = 76\text{ mm}$ and a gap to the cup of $L_{gap} = 6\text{ mm}$. The maximum sample height when filled to the top of the cup is $H_{sample} = 125\text{ mm}$. In this simple design, the angular velocity is provided by a brushless dc servo-motor

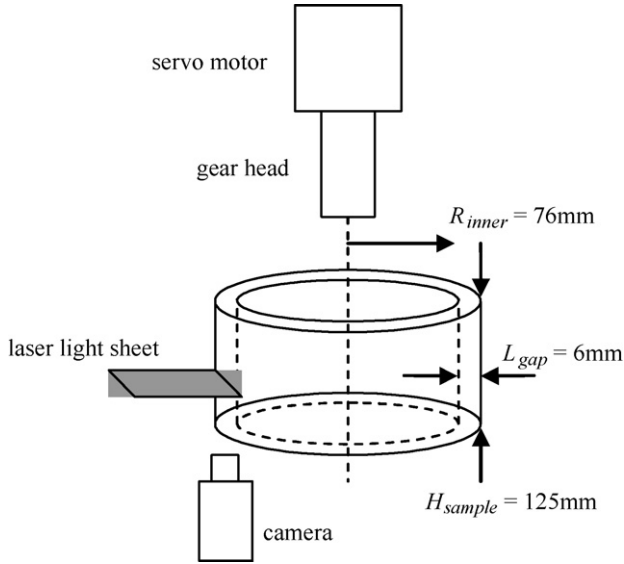


Fig. 5. Schematic diagram of custom built Couette cell with optical access for PIV and birefringence measurements. The diagram is shown with PIV components (camera and laser light sheet) in place.

(ElectroCraft 3622) which is controlled by supplying a reference voltage through a potentiometer (Helipot) via a servo amplifier (AMC BE12A6E) and optical encoder (Servo Systems SSC DA15). Speed reduction of the servo-motor was necessary to achieve steady operation at low shear rates. This was accomplished with a 1000:1 ratio gear-head (Carson 23EP), with vibrations being absorbed by a helical-beam flex-coupling (McMaster Carr) between the gear-head output and the cylindrical input shaft. The end-result is a fully rate-controlled Couette cell. The system was calibrated by timing a number of rotations of the Couette at a given potentiometer setting.

At 8% of the inner Couette cell radius, the gap is on the large side for acceptable curvature effects. This results in a maximum variation in shear rate of 14% across the gap. With such a large gap, one must consider the stability of the flow within the cylindrical geometry. Taylor vortices can form at large rotation rates, resulting in rows of circumferential toroidal vortices within the fluid gap. The critical value for this instability is given by the Taylor number [43]:

$$Ta_{\text{crit}} = r_{\text{inner}} L_{\text{gap}}^3 \frac{\omega_0^2 \rho}{\eta_c^2} \approx 1700. \quad (2)$$

Solving for the critical angular velocity of the spinning bob based on our geometry and using a conservative or worst-case estimate for viscosity of $\eta_c \approx 10^{-2}$ Pa s yields a result of $\omega_0 = 37.5$ rpm. Our motor and 1000:1 gear-head combination reaches a maximum speed of $\omega_{\text{max}} = 6.4$ rpm. In addition to the inertial Taylor instability, analogous elastically driven instabilities may occur in viscoelastic fluids. For an Oldroyd-B fluid, the critical Weissenberg number is defined as [44]:

$$Wi_{\text{crit}} = 5.9 \left(\frac{L_{\text{gap}}}{r_{\text{inner}}} \right)^{1/2} = 21, \quad (3)$$

where the solution is found by substituting the geometric dimensions of our Couette cell. If we once again calculate a worst-case estimate by using the longest relaxation time for the 200 mM solution of $\lambda_M \approx 1.6$ s and a highest possible shear rate of $\dot{\gamma}_{\text{max}} = 9 \text{ s}^{-1}$, we find that the largest Weissenberg number we can probe, $Wi \equiv \dot{\gamma}\lambda = 14$, is less than the critical value in Eq. (3). Therefore, the flow in our geometry will remain fully stable for all of the test fluids and shear rates used in our experiments.

Velocity profiles of the fluid flow inside the gap of the Couette cell are obtained using particle-image velocimetry. To implement this method, a series of images from a high-speed video of the flow are correlated by a PIV analysis routine which has been previously used successfully in our research group [8,45]. The fluids were seeded with 0.050 wt% of neutrally-buoyant, silvered hollow glass spheres with an average size of $50 \mu\text{m}$ (Potters Industries Inc. Spherical 110P8). These spheres are illuminated by an argon-ion laser ($\lambda = 515 \text{ nm}$, National Laser Company) which is passed via fiber optics through a cylindrical lens (Oz Optics) to form a thin light sheet ($<1 \text{ mm}$) which is oriented parallel to the plane of flow in the Couette gap; this is illustrated in Fig. 5. The plane of the light sheet was positioned at an intermediate height within the Couette cell to avoid end-effects from both the bottom of the Couette cell and the free surface on the top of the fluid sample. This illuminated plane was then imaged with a video zoom-microscope lens (Edmund VZM 450i) attached to a high-speed video camera (Phantom v4.2) which was used to capture video at rates up to 400 frames per second. The camera and lens were positioned beneath the glass viewing window in the base of the Couette cell looking up. Video was then converted and analyzed with the PIV correlation routine.

A final resolution of 60 velocity vectors across the 6 mm gap resulted in a spatial resolution of $100 \mu\text{m}$ per vector. This is equivalent to 1.6% of the gap width. Furthermore, use of the high-speed digital video camera subsequently resulted in a very high temporal resolution of 2.5 ms. This is less than 1% of the average Maxwell relaxation times, λ_M , and also significantly smaller than the breakup times, λ_{br} , of all surfactant systems selected for this study. We will present interesting transient flow results based on this temporal resolution in the sections that follow.

Constitutive equations describe the relationship between deformation history and stress in fluid elements [2]. Since most constitutive models differ by the way in which stress is calculated from the deformation history and flow kinematics, measurements of the stress fields within fluid flows are critical in evaluating the models [46]. Flow-induced birefringence allows non-invasive measurements to be made of the average polymer or micelle conformation field in a given geometry with a clear optical path through the device and flow. Optical rheometry measurements are possible in polymeric solutions and wormlike micelles as a direct result of the anisotropy in the index of refraction of the micelle solutions. The index of refraction is different tangent and normal to the polymer backbone or wormlike micelle chain making it possible to measure the orientation and deformation state of the polymers and micelles. In the absence of micelle deformation, there is an equal likelihood of passing normal and tangent to a micelle chain in its random-walk

configuration. Upon the inception of flow, the wormlike micelle is deformed and birefringent. It should be noted that as a line-of-sight technique, these measurements are much easier to interpret and deconvolute when the stress tensor does not vary along the light path. In our experiment, the light will travel down the height of the Couette cell, H_{sample} , and measure the micelle deformation in the $r\theta$ -plane. The resulting optical observables are the difference in the principal value of the refractive index, or the birefringence, $\Delta n'$, and the orientation angle of the principal optical axis with respect to the axis along which deformation is imposed (the shear direction), χ [47]. The stress-optical rule relates these observables to stress tensor components:

$$\Delta n' \sin 2\chi = 2C\tau_{21}, \quad (4)$$

$$\Delta n' \cos 2\chi = C(\tau_{11} - \tau_{22}). \quad (5)$$

Here, C is the stress-optical coefficient. It has been observed that the stress-optical law does not hold for large deformations present in the shear stress plateau region which is a characteristic of shear-banding [12]. For this reason, C was calculated using data at low shear rates, prior to the onset of shear banding and was found to be consistent and applicable for all concentrations. In most optical techniques, birefringence is calculated from measurement of the observable retardation, δ , or the phase difference induced between parallel and perpendicular linear polarization components [46,47]:

$$\delta = \frac{2\pi(\Delta n')H_{\text{sample}}}{\lambda} \quad (6)$$

Here, λ is the wavelength of light used and H_{sample} is the thickness of the sample. Many flow birefringence studies have been performed using Couette cell shear flows [12,14,27,28,42,46] where Eqs. (4) and (5) provide a measure of shear stress and normal stress difference, respectively.

FIB measurements are performed using a polarization modulation method with an optical train shown schematically in Fig. 6. A laser diode with a wavelength of $\lambda = 633$ nm is used as the light source. Light first passes through a polarizer (Oriel) oriented at 90° with respect to the flow direction, a dual-crystal photoelastic modulator (PEM, New Focus 20k) that is being driven at 20 kHz, and a quarter-wave plate (Thorlabs WPMQ05m-633) oriented at 0° . After passing through the sample, the light passes through another quarter-wave plate oriented at 90° , and a polarizer at 45° . The intensity of the final signal is measured by a photodetector (Thorlabs DET210). The measurables from the photodetector are the dc component of the light intensity, I_{dc} , and the amplitude of oscillations of the principle frequency of the PEM and its first harmonic, I_ω and $I_{2\omega}$. The dc component is measured with a pre-amplifier (Signal Recovery 5113) while the oscillation components are measured with a lock-in amplifier (Perkin-Elmer 7265). Analysis of the optical train using Mueller calculus yields the following expressions for the ratios R_ω and $R_{2\omega}$ [46,47]:

$$R_\omega = \frac{I_\omega}{2J_1(A)I_{\text{dc}}} = \sin \delta \cos 2\chi, \quad (7)$$

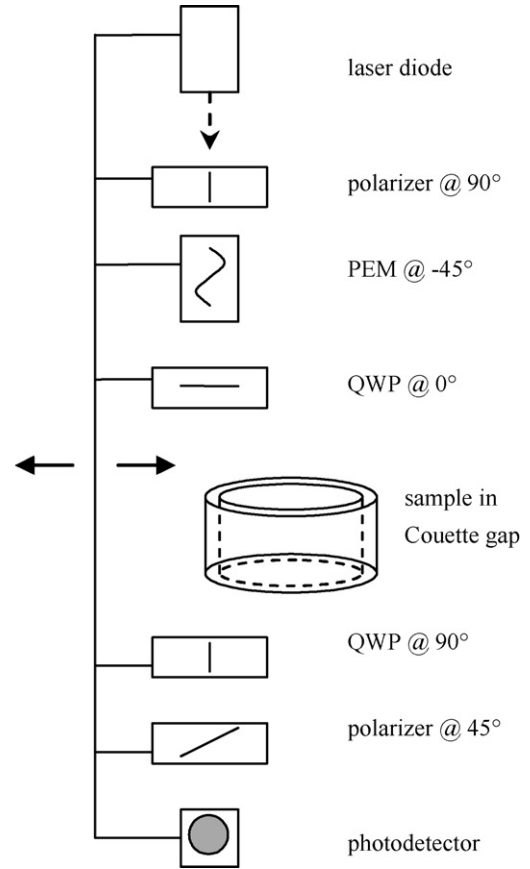


Fig. 6. Schematic of the polarization modulation method optical train, mounted on motor-powered translation stage, used for flow-induced birefringence measurements, both pointwise and transient.

$$R_{2\omega} = \frac{I_{2\omega}}{2J_2(A)I_{\text{dc}}} = -\sin \delta \sin 2\chi, \quad (8)$$

where $J_1(A)$ and $J_2(A)$ are Bessel functions of the first-kind and the amplitude of the PEM oscillations are calibrated such that $J_0(A) = 0$. The values of $J_1(A)$ and $J_2(A)$ are thereby fixed at $J_1(A) = 0.5191$ and $J_2(A) = 0.4317$. From Eqs. (7) and (8), δ and χ can be determined from:

$$\delta = \sin^{-1} \sqrt{R_\omega^2 + R_{2\omega}^2}, \quad (9)$$

$$\chi = \frac{1}{2} \tan^{-1} \left(\frac{R_{2\omega}}{R_\omega} \right) \quad (10)$$

All the components of the optical train depicted in Fig. 6 were mounted on a vertical rail attached to a linear positioning stage (NRC 290TP). This rail was aligned with the Couette flow cell and allowed for translation across the fluid gap. The resulting pointwise FIB measurements are then used to observe development and arrangement of the deformation field within the shear-banded structure of wormlike micelles. In these measurements, the spot size of the laser and the size of the photodetector sensor limit the spatial resolution. The diameter of the laser beam passing through the sample is approximately 0.5 mm, making it possible to take roughly 12 independent birefringence measurements across the gap with each measurement sampling about 8% of the gap.

3. Results and discussion

3.1. Steady velocimetry

It is important to consider the underlying rheology for each surfactant system in the given shear flow. The steady-shear rheology presented in Fig. 4 can be re-plotted in terms of shear stress instead of viscosity. This produces the results shown in Fig. 7, where the stress plateau indicative of shear-banding is apparent for all three experimental solutions. This figure illustrates the operating range of our Couette cell and between all three systems, 50–200 mM, captures the Newtonian regime, the critical plateau value, and values well into the stress plateau. It should also be noted that none of the experiments performed in this study, either controlled shear-rate or stress, exhibited hysteretic top- or bottom-jumping effects. Furthermore, we are able to capture the beginnings of the high-shear branch in the 100 and 200 mM CPyCl/NaSal solutions in shear rheology before the fluid begins to foam and eject from the gap of the shear rheometer.

The first sets of experimental results from the Couette cell are steady velocity profiles for all surfactant concentrations at increasing shear rates. The results shown in Fig. 8 were taken after the flow was allowed to equilibrate for several minutes. It should be noted that later transient experiments showed steady shear-banded flow actually occurred in much less than several minutes; the details will be discussed in the following sections. Each velocity profile shown in Fig. 8 represents an average of at least two distinct experiments, where each experiment contributes several vector fields correlated from a short “snapshot” in time of 0.125 s. In total, each final velocity profile is the average of at least 10 vector fields over multiple experiments. To better validate the trends seen in later transient results, representative error bars indicate the standard error among the vector

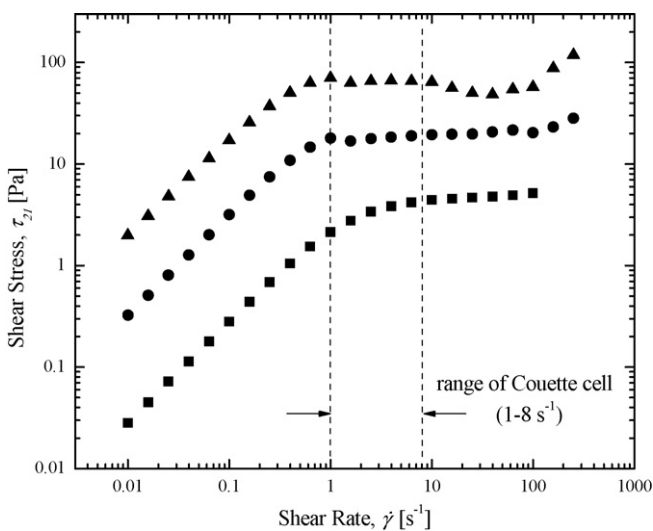


Fig. 7. Steady-shear rheology of CPyCl/NaSal [$R=2$] solutions in 0.1 M NaCl at $T=20^\circ\text{C}$ showing stress plateau behavior, indicative of shear-banding. The data include shear stress for various concentrations: 50/25 mM (\blacksquare), 100/50 mM (\bullet), and 200/100 mM (\blacktriangle); and dashed lines represent the range of the purpose-built Couette cell used in visualization experiments.

fields with 95% certainty. Based on this averaging method, the error bars illustrate the level of both repeatability and very short-time fluctuations. These measurements emphasize that both the position and strength of the multiple shear-bands seems to be relatively steady with time and consistent from one experiment to another. It is possible that excessive averaging could smooth out some subtle features, especially if the Couette has slight imperfections.

The PIV results in Fig. 8 are consistent with the shear rheology shown in Fig. 7. The 50 mM solution shows very little shear-banding until the highest shear rate ($\dot{\gamma} = 8\text{ s}^{-1}$). This shear rate corresponds with the rate at which the shear rheology begins to enter the stress plateau. The 100 mM system begins to show banding at much lower rates. We observe a stacking of low shear-rate branches above $\dot{\gamma} = 3\text{ s}^{-1}$ and an increase in the size of the high shear rate band with increasing average shear rate. The 200 mM system is similar to the 100 mM but the onset of shear-banding is found to occur at a lower shear rate of $\dot{\gamma} = 1\text{ s}^{-1}$. Fig. 8 also highlights the benefits of our high spatial resolution in that the varying size of the high-shear bands can be distinguished and observed to grow from less than 10% of the gap width at high shear rates in the 50 mM to almost 50% in the 200 mM. An additional observation is the appearance of multiple shear-bands in both the 100 and 200 mM results. Specifically, in Fig. 8b for the 100 mM system, between position $y/L=0$ and 0.2, rather than one shear-band with a much higher slope than that which is seen between $y/L=0.2$ and 0.8, we see evidence of multiple bands with the highest slope nearest the inner moving wall at position $y/L=0$. To our knowledge, this is the first observation of multiple shear-bands in the experimental literature for Couette geometry. Multiple bands have been observed using NMR in a cone-and-plate rheometer [48], however, in this geometry, the shear rate is constant across the gap making the choice of location or number of shear-bands unclear. For comparison, Fig. 8d shows the theoretical results for the velocity profiles in the flow between two concentric cylinders with radii R_{inner} and R_{outer} [43], which reduce to:

$$v_{\theta}(r) = \frac{\omega R_{\text{inner}}}{r} \left[\frac{1 - (r/R_{\text{outer}})^2}{1 - (R_{\text{inner}}/R_{\text{outer}})^2} \right], \quad (11)$$

where r is the radial position in the gap and ω is the rotation rate of the inner cylinder. These nearly linear theoretical velocity profiles are the most similar to the 50 mM solution in Fig. 8a, which is not yet fully in the shear-banding region at the imposed shear rates. Closer comparison of the inner wall velocity to the theory does suggest some amount of slip. While it is conceded that PIV results very near the wall may be affected by a slight depletion of both light and particles, the indication of slip is clear and justifies some further investigation. It should be noted that the largest slip is observed at shear rates where shear-banding is clearly present. Within the shear-banding regime, the apparent slip at the wall could be slip, it could be a very narrow high-rate shear-band below the resolution of our PIV, or it could be a combination of both.

The theory was also used to fit the slope of the low shear-rate bands to more accurately determine the critical shear rate, $\dot{\gamma}_{\text{crit}}$,

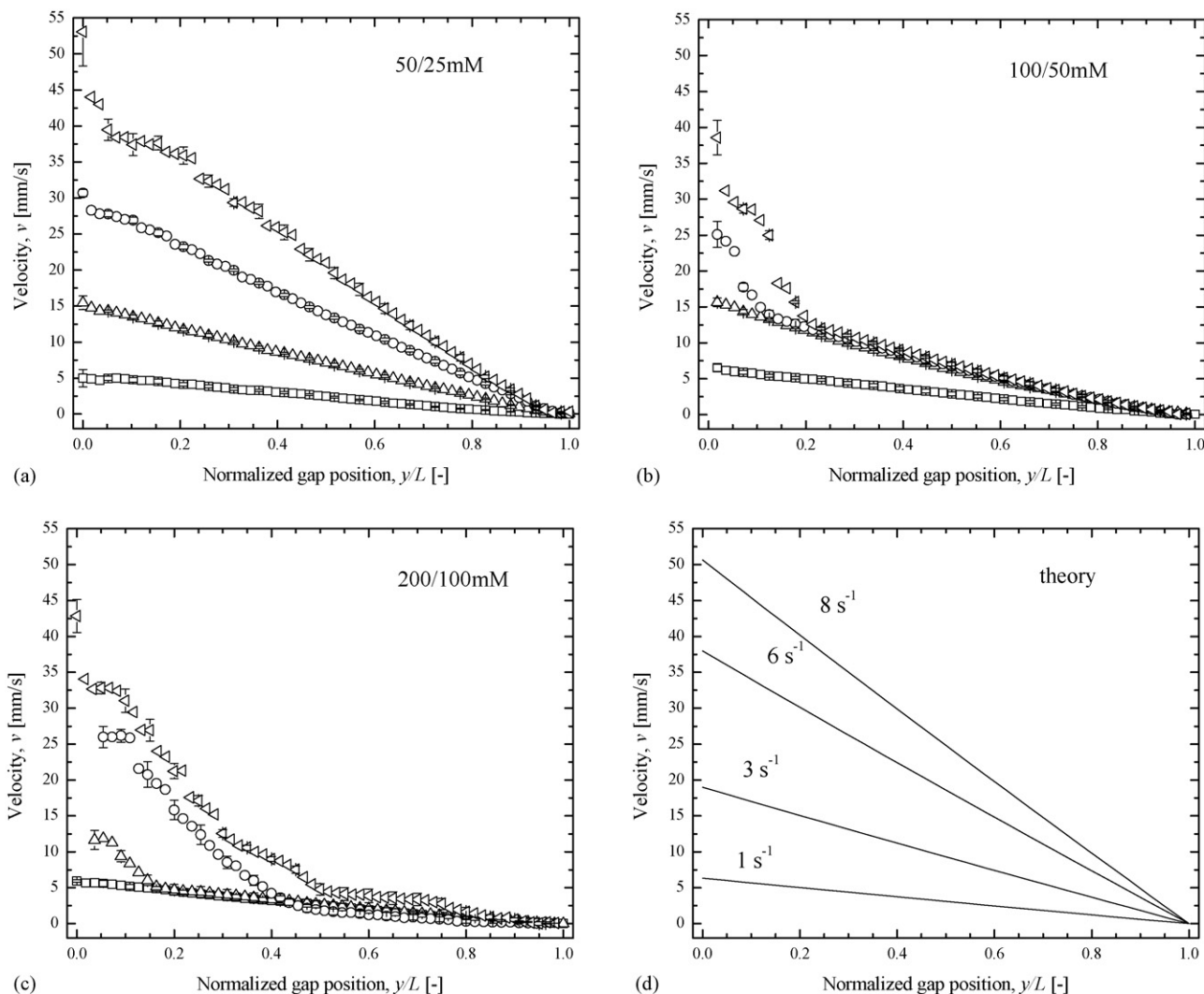


Fig. 8. Steady velocity profiles from PIV experiments showing shear-band development with increasing shear rate. The data for all cases (a)–(c) of varying CPyCl/NaSal concentration, include $\dot{\gamma} = 1 \text{ s}^{-1}$ (\square), 3 s^{-1} (\triangle), 6 s^{-1} (\circ), and 8 s^{-1} (\blacktriangleleft), as well as (d) the theoretical profiles for a stable Newtonian flow in the given Couette geometry. Representative error bars for a 95% standard error have been shown every three data points. In all cases, the moving inner wall is at position $y/L=0$.

for each of the three CPyCl concentrations. This critical shear rate was then used to determine a critical Weissenberg number for the onset of shear-banding, independent of temperature, for each system; the results are included in Table 1.

In a shear-banding flow, the fluid in a given flow exists at multiple shear rates. The velocity profile data was used to calculate the local shear rate within the gap by taking the derivative of the steady velocity using an averaged central difference method [15]. Fig. 9 shows the local shear rate profile at $\dot{\gamma} = 8 \text{ s}^{-1}$ for all three surfactant concentrations. In the lower shear-band, between position $y/L=0.5$ and 1.0 , the shear rate profiles are nearly constant and are in good agreement with the critical shear rate for each concentration found by fitting the low shear rate band steady PIV data. While there is some amount of noise due to the numerical derivative taken on a fairly small number of points, in the high shear-band, the local shear rate results further suggest the existence of multiple shear-bands. The 100 mM data in particular goes from a highly stable low shear-band value of

approximately $\dot{\gamma}(y) = 4 \text{ s}^{-1}$ at $y/L=0.2$, to a high shear-band value of $\dot{\gamma}(y) = 48 \text{ s}^{-1}$, before going back down and up again. Although this further suggests the existence of multiple shear-bands near the moving inner boundary, it is possible that the phenomenon very near the wall is in fact apparent slip. Furthermore, resolving PIV vectors at the inner wall is difficult, and in the calculation of the shear rate profiles the effect is compounded by the low resolution numerical derivative.

3.2. Transient velocimetry

The transient rheology of wormlike micelles has been explored in several previous studies [11,28,34], all with similar results, so we will not present our results here. As expected from a viscoelastic system, transient experiments for a given shear state show an initial underdamped elastic overshoot as the steady rate is instantaneously imposed followed by some longer

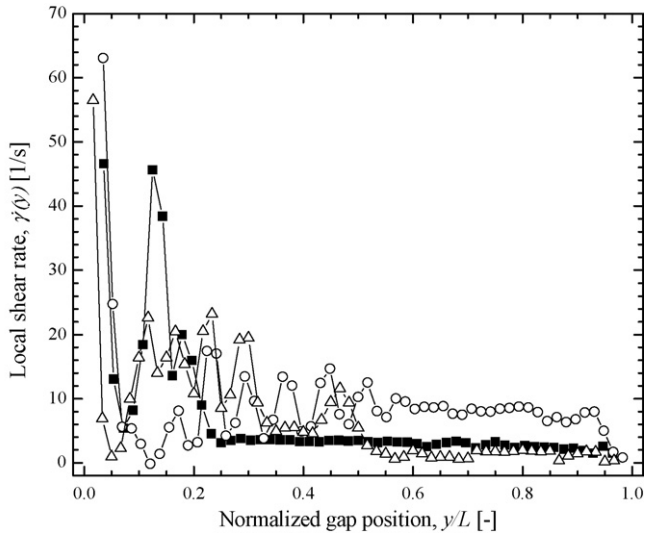


Fig. 9. Local shear rate across the gap, calculated using central difference derivative from steady velocity profiles of CPyCl/NaSal solutions. The data include local shear rate for the three concentrations at a single imposed global shear rate, $\dot{\gamma} = 8 \text{ s}^{-1}$: 50/25 mM (\circ), 100/50 mM (\blacksquare), and 200/100 mM (\triangle); straight lines are included between the data to guide the eye.

time fluctuations. Utilizing a high-speed camera, the goal of this study was to explore the underlying velocity profiles and flow kinematics during the startup of a shear flow. The servomotor used in the Couette cell system was capable of producing a nearly instantaneous startup, and was able to do so with little initial vibration (jerkiness) of the motor.

Transient results for the 50 and 100 mM CPyCl systems are shown in Figs. 10 and 11, respectively. Both sets of results are at a shear rate of $\dot{\gamma} = 8 \text{ s}^{-1}$ and are presented in stages of differing development; the 50 mM exhibits two stages of development, while the 100 mM has four clear stages. On very short time scales, the startup impulse manifests itself in both systems in the form of a propagating damped elastic wave. In Figs. 10a and 11a,

this is observed as a quickly growing velocity profile. At its maximum, the velocity profile is nearly plug-like and has a plateau value close to the known wall velocity, $v_{\text{wall}} = 50 \text{ mm/s}$. From the elastic wave speed defined and calculated in Table 1 for each fluid, we can calculate the time necessary for an elastic wave to transverse the 6 mm gap. The result for the 50 and 100 mM is roughly $t = 0.09$ and 0.04 s , respectively. This calculated time is in excellent agreement with the observed results for the propagation time of the plug velocity profile in both systems. To our knowledge, this result on such short time scales has not been reported in any previous work.

In the next stage of velocity profile development, the elastic wave is well damped and the plug-like profile falls onto the nearly linear profile predicted by theory for a flow in the absence of shear-banding. This occurs on the timescale of less than one Maxwell relaxation time and is observed with both systems. Once again, both systems show excellent agreement between the relaxation times measured with shear rheology in Table 1 and the time at which the first nearly linear velocity profile is observed in the transient experiment. In the case of the 50 mM system, there is no further interesting development beyond the time scale of one relaxation time because the shear band is very small and isolated. From $t = 0.3 \text{ s}$ to 5 min , shown in Fig. 10b, there is little fluctuation in the velocity profile outside of normal noise associated with these experimental measurements. The final profile is nearly linear with an indication of a very small high shear-rate band close to the moving wall, which is captured in the velocity profile at $t = 7 \text{ s}$ but missed in all the others. As suggested in the previous section, this demonstrates how difficult it is to capture the slip velocity at the wall.

The 100 mM system, however, shows some additional features most likely due to the fact that at the imposed shear rates, it is well within the shear-banding plateau region, unlike the 50 mM. In Fig. 11b, after the collapse of the plug-like elastic wave profile but before one Maxwell relaxation time, there is a substantial amount of fluctuation around a nearly linear profile.

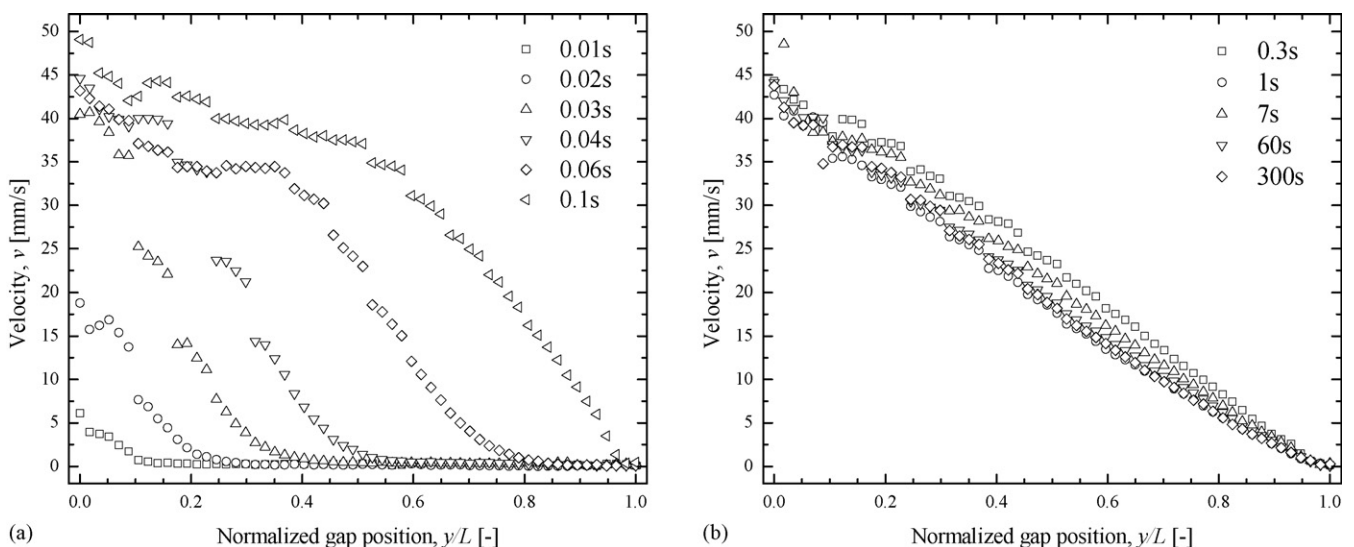


Fig. 10. Transient velocity profiles from a startup experiment with 50/25 mM CPyCl/NaSal system. All data are for an imposed shear rate of $\dot{\gamma} = 8 \text{ s}^{-1}$ and temporal spacing is in seconds. Figures (a) and (b) show a two stage progression in the development of a steady velocity profile.

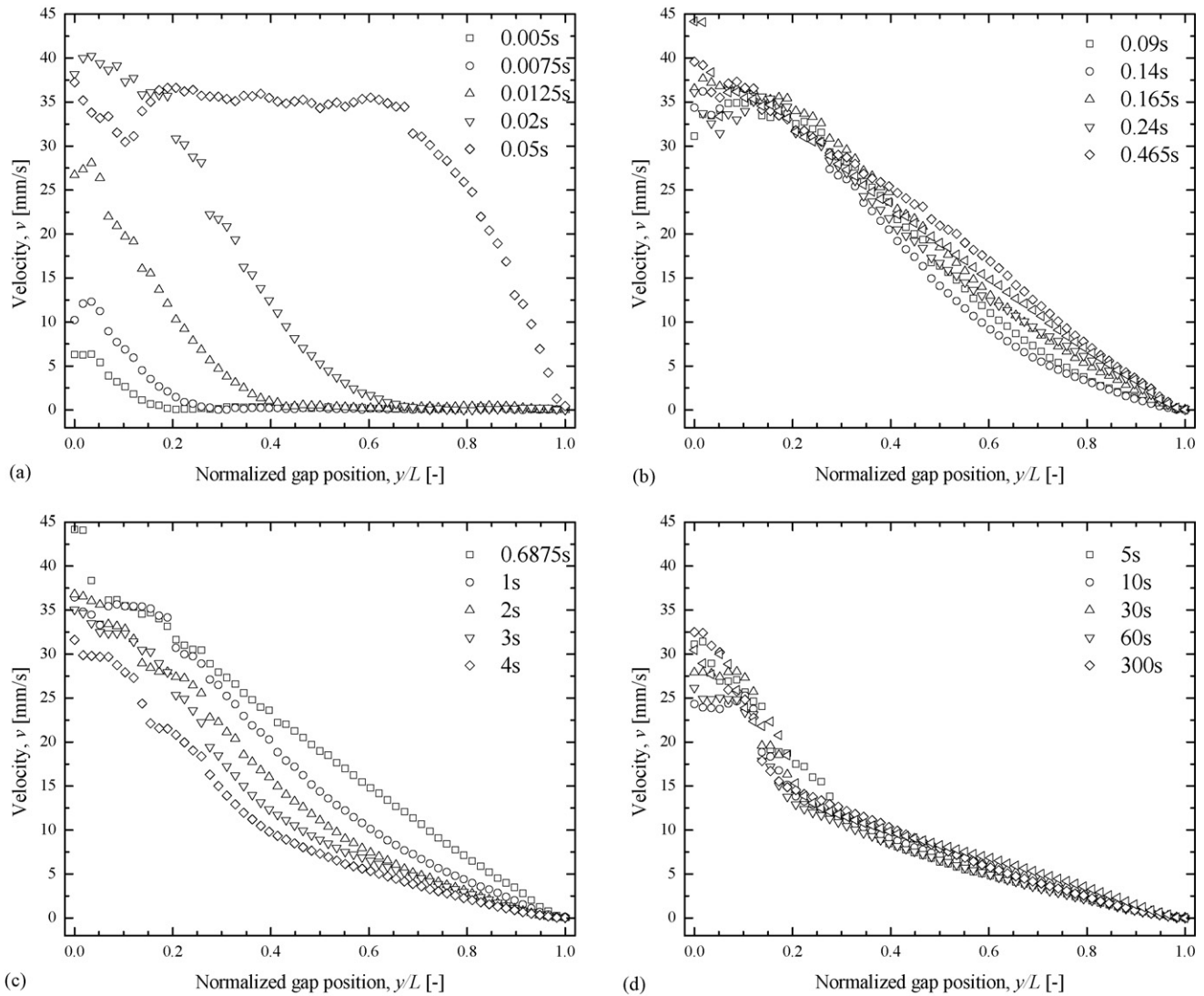


Fig. 11. Transient velocity profiles from a startup experiment with 100/50 mM CPyCl/NaSal system. All data are for an imposed shear rate of $\dot{\gamma} = 8 \text{ s}^{-1}$ and temporal spacing of profiles is in seconds. Figures a–d show a four-stage progression in the development of a shear-banded steady velocity profile.

The fluctuation is not monotonic, but is observed to fluctuate up and down. This is perhaps indicative of some underdamped harmonic in the system. After approximately $t = 0.07 \text{ s}$, the velocity profile begins a monotonic collapse from a nearly linear profile towards the eventual shear-banded profile, as shown in Fig. 11c. At about one relaxation time, $\lambda_{M,100 \text{ mM}} = 1.44 \text{ s}$, the profile is already showing a bend between a low and high shear-band. After three to four Maxwell times, at $t = 5 \text{ s}$, the 100 mM system appears fully banded and remains stable well beyond 5 min, as shown in Fig. 11d. In this final stage, the small fluctuations can be explained by slight imperfections in the Couette cell rather than actual movement of the banded structure.

During the multi-stage development of the shear-banded structure in the 100 mM system, the observed slip velocity increases from $v_{\text{slip}} = 0 \text{ mm/s}$ to almost $v_{\text{slip}} = 20 \text{ mm/s}$ at long times. It should be noted that a number of studies only observe wall slip at some critical value corresponding to a primary stress peak, and otherwise did not observe any slip at all in very similar micellar solutions [16]. Potential reasons for this discrepancy

include aggressive temporal averaging as well as lower spatial resolution.

To better visualize the multiple stage development of the startup flow in the 100 mM CPyCl wormlike surfactant system, a contour map was constructed. In the contour map, both gap position and velocity have been normalized. The full evolution from $t = 0$ to 20 min is shown in Fig. 12 on a logarithmic time scale to highlight the short time behavior. In this map, we see the relatively smooth propagation of the damped elastic wave, which peaks for a very short time, but with an 80% majority of the gap nearly achieving the wall velocity. This quickly settles down with some slight fluctuations that are seen throughout the entirety of the transient experiment. When re-mapped on a linear time scale in Fig. 13, the short time development is obscured, but the stability of the banded profile is evident. The contour levels are much closer to each other near the moving wall (position = 0) and show little fluctuation on long time scales. This long-time velocity profile observation of shear-band stability is in disagreement with the full-field flow birefringence results of Lerouge et

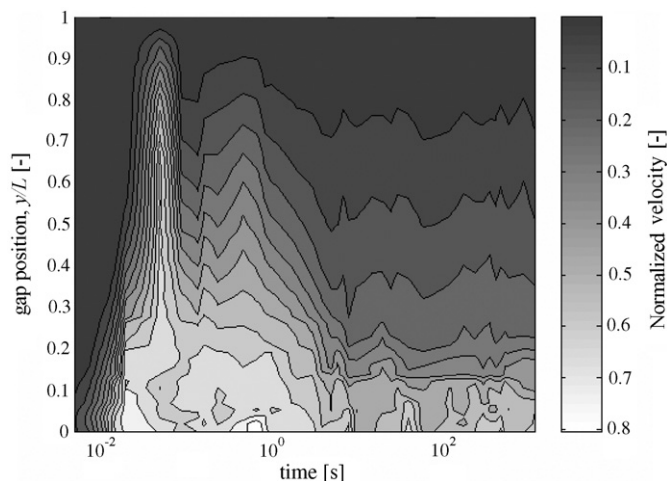


Fig. 12. A contour map of transient velocity profile development from a startup experiment with 100/50 mM CPyCl/NaSal system. All data are for an imposed shear rate of $\dot{\gamma} = 8 \text{ s}^{-1}$. Contours represent the velocity, normalized by that of the moving inner wall, $v_{\text{wall}} = 50 \text{ mm/s}$. This map is plotted on a log time scale to emphasize the early damped elastic wave propagation.

al. [13] that show a large amount of fluctuation and anisotropy on times scales of 100 s and more. It is noted however, that these longtime fluctuations in the birefringence do not coincide with transient stress measurements in a shear rheometer [13], which appear to be stable after short-time development and fluctuation, much like our velocity profiles. This discrepancy between the stress-field as measured optically and the velocity profile development will be addressed by our birefringence results in the following section.

3.3. Steady pointwise birefringence profiles

While high-resolution velocimetry results provide a great deal of insight into the development of a shear-banded flow, knowledge of the underlying micelle deformation fields is essential to the formulation of constitutive models as well as a true understanding of the shear-banding mechanism. To this end, we

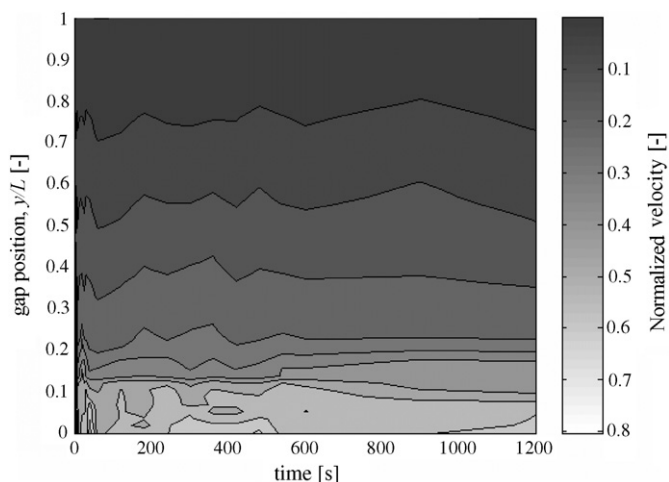


Fig. 13. Same contour map as in Fig. 12, plotted on a linear scale to show long time stability of shear-banded structure within the gap.

acquired both steady and transient flow-induced birefringence measurements in the same Couette cell that we performed the PIV. Velocity profile results have suggested the shear-banded structure in the wormlike system is stable at long times, therefore steady-flow birefringence profiles of the gap can be obtained with relative ease. Startup of flow, however, presents a practical problem. Unlike PIV, quantitative FIB measurements are pointwise rather than full-field. Full-field FIB measurements are possible, and commonly used to show interesting transient results [13]. These full-field FIB measurements are typically images taken through crossed polarizers showing intensity variations within a flow field. These images are only qualitative because they cannot account for changes of incident light intensity for highly dichroic fluids such as wormlike micelle solutions. The modulated FIB system used in our experiments is insensitive to the degree of dichroism because it is a ratiometric technique that explicitly accounts for changes of the intensity of incident light. Unfortunately, instantaneous gap profiles are not possible because the FIB optical train, described earlier and shown in Fig. 6, must be marched across the gap. Gap profiles at equilibrium are easily achieved with excellent spatial resolution. For transient startup results, quantitative FIB measurements are therefore limited to a fixed point in the gap.

The FIB data show interesting results and correlation with the velocity profiles. A full steady-flow characterization was performed with the 50 mM system, and the results are shown in Fig. 14. As expected for this concentration, both the extinction angle and birefringence data show little evidence of shear-banding at low shear rates. At $\dot{\gamma} = 1$ and 2 s^{-1} both profiles are nearly flat across the gap, indicating that the wormlike micelles are in a uniform state of orientation and deformation. The extinction angle in these cases is nearly uniform at, $\chi = 45^\circ$, which is the expected orientation state in a shear flow. As the shear rate increases to the level at which shear-banding should be evident in the 50 mM system, $\dot{\gamma} = 8 \text{ s}^{-1}$, the extinction angle curve shows a pronounced slope of increasing orientation towards the inner rotating wall, at $y/L = 0$. There is some pronounced noise in this data, however, it is clear that near the inner rotating wall in the region of the high shear-band, the worms seem to be more oriented, where $\chi = 0^\circ$ is fully aligned in the flow direction. Comparison of this steady FIB data to the steady PIV data results in an interesting observation. At $\dot{\gamma} = 8 \text{ s}^{-1}$, the extinction angle data for this system suggests that more than 40% of the gap displays a shear-banding variation from a nearly constant orientation. The respective PIV profile (see Fig. 8a), however, only suggests a shear-band in the final 10% of the gap. This inconsistency seems to suggest there is an orientation and deformation threshold at which a change in the morphology corresponds to a shear-band as visualized by PIV.

The data also appear to show that the shear-band as measured by the birefringence is quite diffuse. This is in direct contrast to the velocity profiles which show a very sharp transition from one shear-band to the next. FIB data points included in this study (in Figs. 14 and 15) are an average over a finite spatial increment of several raw data points. The result minimizes noise and also accurately represents the resolution as dictated by the width of the laser beam as it passes through the sample in the Couette

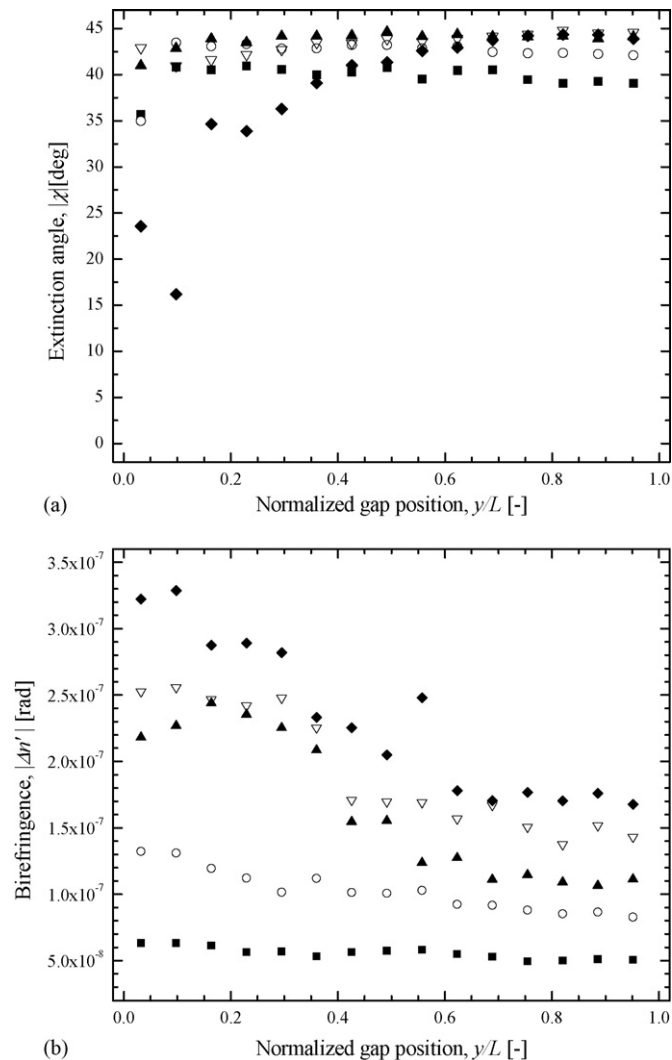


Fig. 14. Steady extinction angle (a) and birefringence data (b) across the Couette cell gap in a fully developed steady flow of the 50/25 mM CPyCl/NaSal system. The data include $\dot{\gamma} = 1 \text{ s}^{-1}$ (■), 2 s^{-1} (○), 4 s^{-1} (▲), 6 s^{-1} (▽), and 8 s^{-1} (◆).

cell. We include this procedural detail to clarify that it is not a moving averaging routine which causes the diffuse transition in the shear-bands.

The birefringence data in Fig. 14b show similar behavior and we see further evidence of an observable change in the micelle deformation field prior to that of the velocity profile. At a shear rate of $\dot{\gamma} = 4 \text{ s}^{-1}$ and above, the birefringence profile changes from nearly constant across the gap, to somewhat dual-natured, with a significantly higher level at the inner rotating wall. According to the shear rheology (see Fig. 7), $\dot{\gamma} = 4 \text{ s}^{-1}$ is well within the non-banding Newtonian regime for this concentration system. This result suggests that there exists an underlying diffuse band that the FIB measurements clearly show is both more highly deformed and oriented than the bulk fluid. This birefringent band is a precursor to the eventual low and high shear-rate bands at shear rates where velocity profiles show a uniform and non-banding result (see Fig. 8a). It should be noted that the birefringence profile, $\Delta n'$, is calculated from the retardation signal using Eq. (6), which has a maximum numerical value of $\delta = \pi/2$.

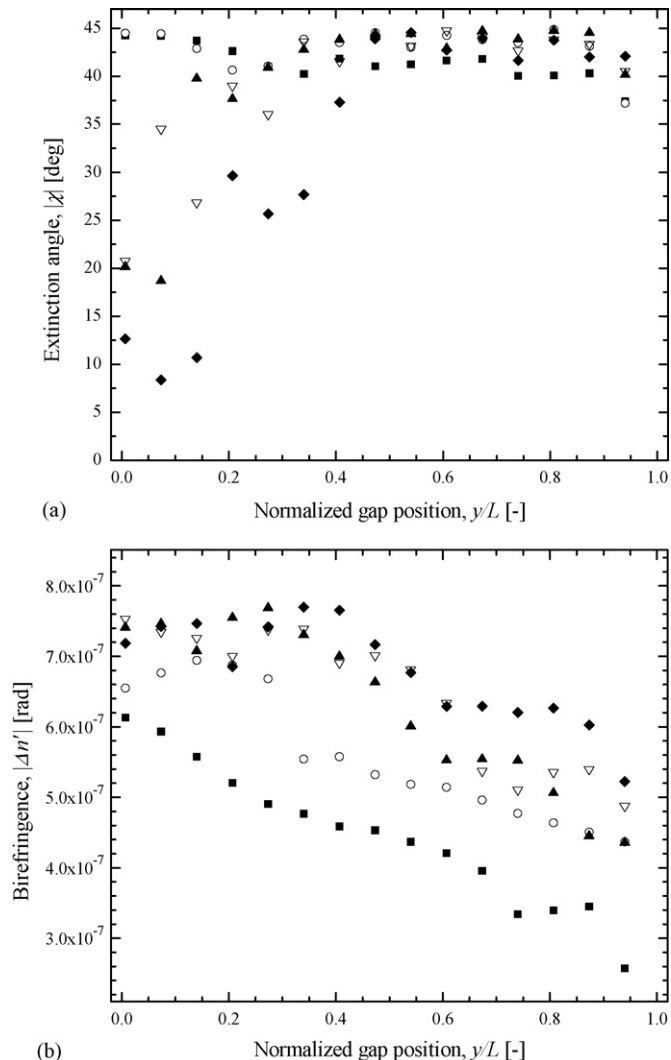


Fig. 15. Steady extinction angle (a) and birefringence data (b) across the Couette cell gap in a fully developed steady flow of the 100/50 mM CPyCl/NaSal system. The data include $\dot{\gamma} = 1 \text{ s}^{-1}$ (■), 2 s^{-1} (○), 4 s^{-1} (▲), 6 s^{-1} (▽), and 8 s^{-1} (◆).

Unlike the extinction angle, which is a measure of orientation and by symmetry conveys no difference beyond the range from $\chi = 0$ to 45° , the retardation signal goes through several orders. In our experiment, the light has a relatively long path through the birefringent sample and must be unwrapped through several orders to give an accurate result. This experimental aspect makes it more difficult to acquire FIB profile measurements across the gap of the more concentrated and therefore more strongly birefringent 100 and 200 mM CPyCl systems.

Fig. 15 shows the steady FIB gap profile results for the 100 mM system. Despite the extra analysis required to unwrap this system, the results are quite good and in agreement with the trends observed in the 50 mM system. The extinction angle data is nearly constant at the expected shear flow orientation of $\chi = 45^\circ$ at low shear rates before showing a pronounced slope towards $\chi = 0^\circ$ at shear rates above $\dot{\gamma} = 2 \text{ s}^{-1}$. As with the 50 mM system, at the highest shear rate of $\dot{\gamma} = 8 \text{ s}^{-1}$, the pronounced slope in the extinction angle profile accounts for over 40% of the gap while the high shear-band in the velocity profile

(see Fig. 8b) is seen in only 20% of the gap. This is further evidence that the micelles become aligned over a broad diffuse region and do not exhibit the sharp transition observed between the high and low shear-rate bands. Additionally, the onset of micelle deformation and alignment again occurs significantly farther from the outer wall than the discontinuity observed in the velocity profile. By comparing the size of the shear bands in Fig. 8b to that of the trend in the extinction angle in Fig. 15a, there is a reasonable correlation suggesting that $\chi \simeq 25^\circ$ is a critical value of orientation for the wormlike micelles above and below which exist the low and high shear-rate bands, respectively. We do not have a physical interpretation of this phenomenon. It is our hope that comparison with constitutive models might shed some light on this observation. The birefringence data in Fig. 15b for the 100 mM system also exhibit the same trend of increasing deformation in the micelles near the inner moving wall. Furthermore, at high shear rates the birefringence appears to approach a plateau in the maximum value of $\Delta n' = 7.5 \times 10^{-7}$ rad in the high shear-rate band. This value appears to be independent of shear rate, suggesting that the deformation, orientation and morphology of the micelles in the high shear-rate band are independent of bulk shear rate. The FIB data from the low shear-rate band is slightly more complicated. Because of the diffusive nature of the shear-band, even though the velocity profile is not disturbed, the micelles are still deformed beyond the location of the shear-band observed in the velocity profile.

If the birefringence is converted to a stress using the stress-optical coefficient and Eq. (4), the resulting overall shear stress levels are in very good agreement with the observed shear stress from the bulk rheology shown in Fig. 7. As mentioned previously, however, using this calculation to produce a full shear stress profile within the Couette gap would be misleading. It is reassuring that the shear stress levels coincide between our experiments, but the high shear rate data is, at best, an estimated result based on the fact that the stress-optical law most likely does not hold for shear-banded regions with large micelle deformations [12].

3.4. Transient FIB

A representative transient FIB measurement is shown in Fig. 16 for the 100 mM CPyCl system. In order to make a comparison with the steady gap profile experiments discussed in the previous section, the optical train was positioned at two points in the gap: near the inner rotating wall, $y/L=0.10$, to capture the high shear-band and near the fixed outer wall, $y/L=0.80$, for the low shear-band. At these two points, the birefringence signal was monitored during a startup experiment. An interesting observation of the data of Fig. 16 is the existence of two distinct levels of birefringence independent of shear rate, and coinciding with the two points of measurement in the gap; a high level near the rotating inner wall and a lower level near the outer wall. Based on the shear rheology in Fig. 7, the 100 mM is within the shear-banding plateau at all shear rates for the experiment in Fig. 16. As expected, the results show that the wormlike micelles near the inner wall are more highly deformed than those in the

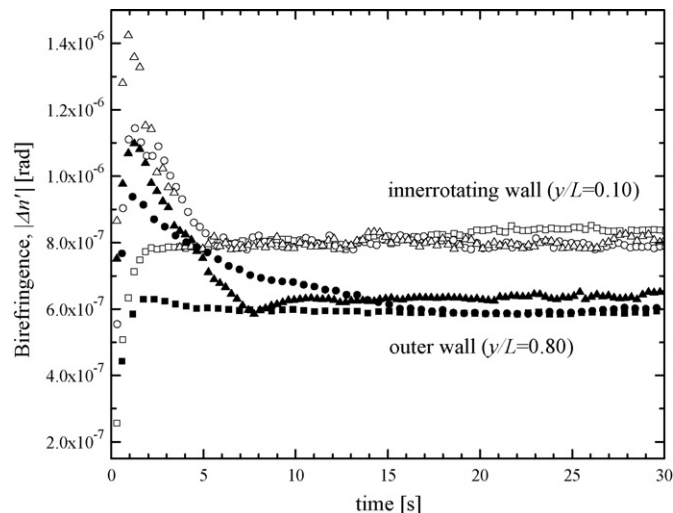


Fig. 16. Transient birefringence data for the 100/50 mM CPyCl/NaSal system. The data include $\dot{\gamma} = 2 \text{ s}^{-1}$ (■), 4 s^{-1} (●), and 6 s^{-1} (▲), with data for the outer fixed wall (filled symbols) and inner rotating wall (open symbols).

outer portion of the gap. However, a more insightful result is that this dual-state arrangement is independent of the imposed shear-rate; all three shear rates eventually settle to the same birefringence level based only on gap position. As a good verification of our experimental results for the 100 mM CPyCl system, we observe that the final birefringence in the transient experiments (Fig. 16) agrees very well with the steady-flow gap profiles (Fig. 15), where for both experiments $\Delta n'_{y/L=0.10} \simeq 8 \times 10^{-7}$ and $\Delta n'_{y/L=0.80} \simeq 6 \times 10^{-7}$, for the shear rates imposed. This result is yet another visualization of the formation of distinct high and low shear-bands. Furthermore, it strongly supports the shear-banding plateau theory wherein the high and low shear-rate bands vary in size and reorganize themselves in terms of shear rate according to the lever rule, as described by Eq. (1), but the stress levels are fixed. This observation is also consistent with the steady-flow experiments where we see distinct and uniform stress levels at each wall but the shear-band transition is diffuse.

At low shear rates, the transient FIB measurements also collapse on a single birefringence value. However, as the high shear-rate band grows with increasing shear rate, an increase in the birefringence can be observed well before the location at which the high shear-rate band moves past the location of the birefringence probe. This rise in the birefringence is due to the nature of the shear-band which can be seen explicitly in the spatially resolved FIB plots in Fig. 15b. Additionally, a close inspection of the outer wall data taken at $\dot{\gamma} = 6 \text{ s}^{-1}$ in Fig. 16 shows that the birefringence originally collapses to a value consistent with the $\dot{\gamma} = 2 \text{ s}^{-1}$ and 4 s^{-1} experiments. Following this, after about 7 s, it begins to grow again and obtains its final value after 12–13 s. These timescales correspond to the timescale for growth and formation of the shear-band observed in the transient PIV measurements shown in Fig. 11.

The general shape of the birefringence history in all cases is fairly typical for a viscoelastic system; there is an initial overshoot with a damped relaxation on a timescale that agrees with

that seen in transient stress experiments [11,28,34]. The initial overshoot becomes higher as shear rate increases, and is highest at the inner wall for each pair of birefringence sweeps. This result is consistent with the higher deformation level at the moving wall, and may simply suggest more dramatic dynamics at that point in the gap. In terms of timescale, the overshoot occurs on the order of a Maxwell relaxation time, thereby correlating with some early time dynamics observed in the velocity-profile development. The higher shear rate sweeps in Fig. 16 also show some relatively long time relaxation after the initial overshoot. At $\dot{\gamma} = 4$ and 6 s^{-1} , near the inner moving wall, the relaxation to a steady deformation level takes approximately $t = 5 \text{ s}$, or several Maxwell times. This result is in good agreement with the multi-stage transient velocity profile development in Fig. 11. Our steady-flow FIB results can once again be used to better interpret the dynamics seen in the transient experiment. For $\dot{\gamma}_{y/L=0.80} = 6 \text{ s}^{-1}$, there is a slight undershoot in the data as the birefringence approaches a lower shear-rate value before jumping back up to the expected level as the deformation ahead of the diffuse shear band reaches it.

4. Conclusions

Surfactant micellar solutions, with their varying morphology and unique ability to behave as living polymers, makes them very interesting subjects in the study of viscoelastic systems. The experiments performed in this study have provided a comprehensive and highly resolved visualization of shear-banding and the underlying deformation and orientation. Gap profiles of a Couette cell in a steady-shear flow provide insight about the size and location of high and low shear-bands. High spatial resolution within these gap profiles has also allowed us to observe multiple high shear-rate bands near the inner moving wall. By comparing the velocity and birefringence profiles from the steady-flow experiments, it is observed that the sharp transition seen in PIV is preceded by a much larger and diffuse transition in the birefringence or underlying deformation in the wormlike micelles. We observe a critical orientation that coincides with the transition from high to low shear-rate band levels. Whether this value is indicative of a phase transition, as suggested by several researchers as the underlying cause for shear-banding is unclear, however, it is clear that there is a critical change in arrangement and perhaps morphology that results in the distinct shear bands seen in various visualizations, including PIV profiles. Our transient experiments, which are resolved at very short timescales, have demonstrated the existence of a propagating damped elastic wave, as well as interesting dynamics prior to the organization of shear-bands. Together, the steady and transient results have helped to interpret the evolution of shear-bands in terms of the visualized sharp band formation and how it is connected with the underlying and much more diffuse deformation and orientation of the micelles. This final observation is very interesting and further investigation including correlation with constitutive models is anticipated to result in a greater understanding of the shear-banding phenomenon.

Acknowledgements

This experimental work was supported by funding from the National Science Foundation (DMS-0406224). We would also like to thank Pamela Cook, Gareth McKinley, Christopher Pipe, Louis Rossi, and Paula Vasquez for productive discussions, assistance and collaboration on this project.

References

- [1] S. Kefi, J. Lee, T. Pope, P. Sullivan, E. Nelson, A. Hernandez, T. Olsen, M. Parlar, B. Powers, A. Roy, A. Wilson, A. Twynam, Expanding applications for viscoelastic surfactants, *Oilfield Rev.* (2004) 10–16.
- [2] R.G. Larson, *The Structure and Rheology of Complex Fluids*, Oxford University Press, New York, 1999.
- [3] M. Cates, S. Candau, Statics and dynamics of worm-like surfactant micelles, *J. Phys.: Condens. Matter* 2 (1990) 6869–6892.
- [4] H. Rehage, H. Hoffman, Viscoelastic surfactant solutions: model systems for rheological research, *Mol. Phys.* 74 (1991) 933–973.
- [5] J.I. Escalante, E.R. Macias, F. Bautista, J.H. Perez-Lopez, J.F.A. Soltero, J.E. Puig, O. Manero, Shear-banded flow and transient rheology of cationic wormlike micellar solutions, *Langmuir* 19 (2003) 6620–6626.
- [6] M. Cates, Flow behaviour of entangled surfactant micelles, *J. Phys.: Condens. Matter* 8 (1996) 9167–9176.
- [7] I.A. Kadoma, J.W. van Egmond, Flow-induced nematic string phase in semidilute wormlike micelle solutions, *Phys. Rev. Lett.* 80 (1998) 5679–5682.
- [8] S. Chen, J.P. Rothstein, Flow of a wormlike micelle solution past a falling sphere, *J. Non-Newtonian Fluid Mech.* 116 (2004) 205–234.
- [9] J.P. Rothstein, Transient extensional rheology of wormlike micelle solutions, *J. Rheol.* 47 (2003) 1227–1247.
- [10] R.W. Mair, P.T. Callaghan, Observation of shear banding in worm-like micelles by NMR velocity imaging, *Europhys. Lett.* 36 (1996) 719–724.
- [11] J. Berret, Transient rheology of wormlike micelles, *Langmuir* 13 (1997) 2227–2234.
- [12] J. Lee, G. Fuller, N. Hudson, X. Yuan, Investigation of shear-banding structure in wormlike micellar solution by point-wise flow-induced birefringence measurements, *J. Rheol.* 49 (2005) 537–550.
- [13] S. Lerouge, J.-P. Decruppe, J.-F. Berret, Correlations between rheological and optical properties of a micellar solution under shear-banding flow, *Langmuir* 16 (2000) 6464–6474.
- [14] J.-P. Decruppe, S. Lerouge, J.-F. Berret, Insight in shear banding under transient flow, *Phys. Rev. E* 63 (2001) 022501.
- [15] A.F. Mendez-Sanchez, J. Perez-Gonzalez, L. de Vargas, J.R. Castrejon-Pita, A.A. Castrejon-Pita, G. Huelzel, Particle image velocimetry of the unstable capillary flow of a micellar solution, *J. Rheol.* 47 (2003) 1455–1466.
- [16] Y.T. Hu, A. Lips, Kinetics and mechanism of shear banding in an entangled micellar solution, *J. Rheol.* 49 (2005) 1001–1027.
- [17] J.-B. Salmon, A. Colin, S. Manneville, Velocity profiles in shear-banding wormlike micelles, *Phys. Rev. Lett.* 90 (2003), 228303-1,4.
- [18] J.-F. Berret, D. Roux, G. Porte, P. Lindner, Shear-induced isotropic-to-nematic phase transition in equilibrium polymers, *Europhys. Lett.* 25 (1994) 521–526.
- [19] M.W. Liberatore, F. Nettesheim, N.J. Wagner, L. Porcar, Spatially resolved smallangle neutron scattering in the 1-2 plane: a study of shear-induced phase-separating wormlike micelles, *Phys. Rev. E* 73 (2006).
- [20] M. Britton, R. Mair, R. Lambert, P. Callaghan, Transition to shear banding in pipe and Couette flow of wormlike micellar solutions, *J. Rheol.* 43 (1999) 897–909.
- [21] M. Doi, S.F. Edwards, *The Theory of Polymer Dynamics*, Clarendon Press–Oxford University Press, Oxford [Oxfordshire], New York, 1986.
- [22] N. Spenley, M. Cates, T. McLeish, Nonlinear rheology of wormlike micelles, *Phys. Rev. Lett.* 71 (1993) 939–942.
- [23] N.A. Spenley, X.F. Yuan, M.E. Cates, Nonmonotonic constitutive laws and the formation of shear-banded flows, *J. Phys. II France* 6 (1996) 551–571.

- [24] L. Jupp, X.F. Yuan, Dynamic phase separation of a binary polymer liquid with asymmetric composition under rheometric flow, *J. Non-Newtonian Fluid Mech.* 124 (2004) 93–101.
- [25] L. Jupp, T. Kawakatsu, X.F. Yuan, Modeling shear-induced phase transitions of binary polymer mixtures, *J. Chem. Phys.* 119 (2003) 6361–6372.
- [26] X.F. Yuan, L. Jupp, Interplay of flow-induced phase separations and rheological behavior, *Europhys. Lett.* 60 (2002) 691–697.
- [27] E. Cappalaere, J. Berret, J. Decruppe, R. Cressely, P. Lindner, Rheology, birefringence, and small-angle neutron scattering in a charged micellar system: evidence of a shear-induced phase transition, *Phys. Rev. E* 56 (1997) 1869–1878.
- [28] J.-F. Berret, G. Porte, J.-P. Decruppe, Inhomogeneous shear flows of wormlike micelles: a master dynamic phase diagram, *Phys. Rev. E* 55 (1997) 1668–1676.
- [29] J. Berret, D. Roux, G. Porte, Isotropic-to-nematic transition in wormlike micelles under shear, *J. Phys. II France* 4 (1994) 1261–1279.
- [30] P. Callaghan, M. Cates, C. Rofe, J. Smeulders, A study of the “spurt effect” in wormlike micelles using nuclear magnetic resonance microscopy, *J. Phys. II France* 6 (1996) 375–393.
- [31] A.F. Mendez-Sanchez, M.R. Lopez-Gonzalez, V.H. Rolon-Garrido, J. Perez-Gonzalez, L. de Vargas, Instabilities of micellar systems under homogeneous and nonhomogeneous flow conditions, *Rheol. Acta* 42 (2003) 56–63.
- [32] V. Rolon-Garrido, J. Perez-Gonzalez, L.V.A. Montalban, Vane rheometry of an aqueous solution of worm-like micelles, *Revisita Mexicana De Fisica* 49 (2003) 40–44.
- [33] B.M. Santibanez, F.R. Gonzalez, J.L.V.A.M. Perez-Gonzalez, E.M. Garcia, Qualitative analysis of the capillary flow stability of spurling materials by using transmitted light intensity measurements, *Revisita Mexicana De Fisica* 50 (2004) 562–568.
- [34] C. Grand, J. Arrault, M. Cates, Slow transients and metastability in wormlike micelle rheology, *J. Phys. II France* 7 (1997) 1071–1086.
- [35] L.R. Rossi, G. McKinley, L.P. Cook, Slippage and migration in Taylor-Couette flow of a model for dilute wormlike micellar solutions, *J. Non-Newtonian Fluid Mech.* 136 (2006) 19–92.
- [36] L.P. Cook, L.R. Rossi, Slippage and migration in models of dilute wormlike micellar solutions and polymeric fluids, *J. Non-Newtonian Fluid Mech.* 116 (2004) 347–369.
- [37] F. Kern, P. Lemarechal, S. Candau, M. Cates, Rheological properties of semidilute and concentrated aqueous solutions of cetyltrimethylammonium bromide in the presence of potassium bromide, *Langmuir* 8 (1992) 437–440.
- [38] J.-F. Berret, J. Appell, G. Porte, Linear rheology of entangled wormlike micelles, *Langmuir* 9 (1993) 2851–2854.
- [39] I.A. Kadoma, C. Ylitalo, J.W. vanEgmond, Structural transitions in wormlike micelles, *Rheol. Acta* 36 (1997) 1–12.
- [40] F. Kern, F. Lequeux, R. Zana, S. Candau, Dynamical properties of salt-free viscoelastic micellar solutions, *Langmuir* 10 (1994) 1714–1723.
- [41] R. Granek, M. Cates, Stress relaxation in living polymers: results from a Poisson renewal model, *J. Chem. Phys.* 96 (1992) 4758–4767.
- [42] S.-P. Chen, L.A. Archer, Relaxation dynamics of salt-free polyelectrolyte solutions using flow birefringence and rheometry, *J. Polym. Sci.: Polym. Phys.* 37 (1999) 825–835.
- [43] F.M. White, *Viscous Fluid Flow*, McGraw-Hill, New York, 1991.
- [44] R.G. Larson, Instabilities in viscoelastic flows, *Rheol. Acta* 31 (1992) 213–263.
- [45] J. Ou, J.P. Rothstein, Direct velocity measurements of the flow past drag-reducing ultrahydrophobic surfaces, *Phys. Fluids* 17 (2005).
- [46] J.M. Li, W.R. Burghardt, Flow birefringence in axisymmetrical geometries, *J. Rheol.* 39 (1995) 743–766.
- [47] G.G. Fuller, *Optical Rheometry of Complex Fluids*, Oxford University Press, New York, 1995.
- [48] M.M. Britton, P.T. Callaghan, Two-phase shear band structures at uniform stress, *Phys. Rev. Lett.* 78 (1997) 4930–4933.